





RESEARCH ARTICLE | OCTOBER 10 2023

Phase composition of polycrystalline HfN_x ($0.45 \leq x \leq 1.60$) and effects of low-energy ion irradiation on microstructure, texture, and physical properties **FREE**

Special Collection: [Celebrating the Achievements and Life of Joe Greene](#)

Hwan-Seok Seo ; Taeyoon Lee ; Hyungjun Kim ; Ivan Petrov ; J. E. Greene



J. Vac. Sci. Technol. A 41, 063406 (2023)

<https://doi.org/10.1116/6.0003072>



View
Online



Export
Citation

CrossMark



HIDEN
ANALYTICAL

Instruments for Advanced Science

- Knowledge
- Experience
- Expertise

Click to view our product catalogue

Contact Hiden Analytical for further details:
 www.HidenAnalytical.com
 info@hiden.co.uk



Gas Analysis

- ▶ dynamic measurement of reaction gas streams
- ▶ catalysis and thermal analysis
- ▶ molecular beam studies
- ▶ dissolved species probes
- ▶ fermentation, environmental and ecological studies



Surface Science

- ▶ UHV TPD
- ▶ SIMS
- ▶ end point detection in ion beam etch
- ▶ elemental imaging - surface mapping



Plasma Diagnostics

- ▶ plasma source characterization
- ▶ etch and deposition process reaction kinetic studies
- ▶ analysis of neutral and radical species



Vacuum Analysis

- ▶ partial pressure measurement and control of process gases
- ▶ reactive sputter process control
- ▶ vacuum diagnostics
- ▶ vacuum coating process monitoring

Phase composition of polycrystalline HfN_x ($0.45 \leq x \leq 1.60$) and effects of low-energy ion irradiation on microstructure, texture, and physical properties

Cite as: J. Vac. Sci. Technol. A 41, 063406 (2023); doi: 10.1116/6.0003072

Submitted: 17 August 2023 · Accepted: 18 September 2023 ·

Published Online: 10 October 2023



View Online



Export Citation



CrossMark

Hwan-Seok Seo,^{1,a)} Taeyoon Lee,² Hyungjun Kim,² Ivan Petrov,³ and J. E. Greene^{3,b)}

AFFILIATIONS

¹Department of Materials Science and Engineering, Yonsei University, 50 Yonsei-ro, Seodaemun-gu, Seoul 03722, Republic of Korea

²School of Electrical and Electronic Engineering, Yonsei University, 50 Yonsei-ro, Seodaemun-gu, Seoul 03722, Republic of Korea

³Materials Research Laboratory and Materials Science Department, University of Illinois, 104 South Goodwin, Urbana, Illinois 61801

Note: This paper is part of the Special Topic Collection Celebrating the Achievements and Life of Joe Greene.

^{a)}Electronic mail: hseo88@yonsei.ac.kr

^{b)}Deceased October 10, 2022.

ABSTRACT

We have investigated the phase composition of HfN_x as a function of x and the effects of low-energy ion irradiation on the microstructure and physical properties of polycrystalline layers grown on SiO_2 at 350°C by ultrahigh vacuum reactive dc magnetron sputtering of Hf in mixed N_2/Ar discharges. X-ray diffraction and Rutherford backscattering spectrometry results show that the phases obtained in polycrystalline HfN_x layers with increasing x are hcp-structure α -HfN ($x \lesssim 0.6$); multiphase mixtures consisting of α -Hf, NaCl-structure δ -HfN, rhombohedral ϵ - Hf_3N_2 , and/or ζ - Hf_4N_3 ($0.6 \lesssim x \lesssim 0.9$); δ -HfN single phase ($0.9 \lesssim x \lesssim 1.3$); and mixtures of δ -HfN and higher nitrides ($x \gtrsim 1.3$). HfN_x layers with $0.9 \lesssim x \lesssim 1.2$ grown under mild ion irradiation (incident ion energy $E_i \approx 7$ eV and ion-to-Hf flux ratios $J_i/J_{\text{Hf}} = 1-3$) are underdense with mixed orientation, low in-plane stress, and rough surface morphology due to limited adatom mobilities resulting in kinetic roughening and atomic shadowing during film growth. However, the use of intense ion irradiation ($E_i = 25$ eV and $J_i/J_{\text{Hf}} = 4-20$) results in HfN_x layers, which are fully dense with strongly 111-oriented texture, compressive in-plane stress, and smooth surfaces due to ion irradiation enhanced adatom surface mobilities. In addition, the latter films have lower resistivity and higher hardness. For stoichiometric δ -HfN layers, ρ decreases from 69.7 to $35.2 \mu\Omega \text{ cm}$ and H increases from 22.1 to 27.4 GPa, with increasing ion-irradiation intensity. However, for HfN_x layers with $1.2 \lesssim x \lesssim 1.6$, the correspondingly higher steady state atomic N surface coverages during deposition alter growth kinetics in favor of 001 texture with a fully dense structure and compressive in-plane stress.

Published under an exclusive license by the AVS. <https://doi.org/10.1116/6.0003072>

I. INTRODUCTION

Polycrystalline transition-metal (TM) nitride thin films, typically grown by reactive sputter deposition, have been used in a variety of applications, including hard wear-resistant coatings on tools, diffusion barriers and electrodes for gate and capacitor structures in integrated circuits and resistors, mask layers for x-ray lithography, and decorative coatings. Among the large family of TM-nitrides, the group-IVB members TiN and ZrN have elicited

particular interest because of their low electrical resistivity ($\rho < 20 \mu\Omega \text{ cm}$), due to partially filled TM d-orbitals,¹ and their distinctive gold color, as a result of interband transitions combined with a high reflectance in the red and infrared.^{2,3} However, less is known about the properties of a related group-IVB nitride, HfN.

The physical properties of HfN_x and its suitability for a given application are strongly affected by microstructural attributes, such as grain size and shape (equiaxed versus columnar), porosity,

defect density, and texture. Thus, we anticipate that understanding and controlling microstructural evolution during the deposition of polycrystalline HfN_x will be crucial to the development of this material for future applications.

The majority of TM nitride applications require low film growth temperatures, $T_s \leq 450$ °C [i.e., $T_s/T_m \leq 0.2$ for HfN, where T_m is the melting point, 3660 K (Ref. 4)], in order to, for example, avoid overtempering steel cutting-tool substrates or exceeding the tight thermal budgets associated with Si-based device fabrication. Consequently, ion-assisted film growth, in which ion energy E_i and incident ion-to-metal atom flux ratio J_i/J_{Me} are fundamental parameters, is often employed to control TM nitride film microstructure. Momentum transfer to the lattice during deposition can have a large, and often dominant, influence on adatom mobilities, film nucleation rates, coalescence, column growth, solute solubilities, and residual stresses.^{5,6}

While E_i is easily controlled during conventional dc magnetron sputtering (DCMS) through the use of substrate bias, J_i/J_{Me} cannot be varied independently. Thus, most studies on the effects of ion irradiation during film growth have concentrated exclusively on the role of E_i , with J_i/J_{Me} either constant or uncontrolled, and typically of the order of 0.5–1. The use of E_i values significantly above bulk lattice displacement thresholds, 20–40 eV depending on the materials system (i.e., ion mass and layer composition), leads to film densification and a less pronounced columnar microstructure, compared to films grown with lower ion energies. However, these advantages extract a steep price. In the case of TiN and Ti_{1-x}Al_xN growth, for example, the use of incident N₂⁺ energies $E_i > 25$ eV results in the trapping of accelerated ions, residual lattice defects, and the development of very high compressive stresses.^{7–9}

Recently, high power impulse magnetron sputtering (HiPIMS) has been used extensively to deposit dense films at low temperatures as it generates a high degree ionization of the sputtered species flux with energy distribution of both target and gas ion, extending well above 50 eV.^{10–12}

Thorsteinnsson and Gudmundsson¹³ systematically studied reactive HiPIMS and DCMS deposition of HfN films in Ar/N₂ discharges as a function of nitrogen fraction in the gas, growth temperature, and duty cycle. They found that DCMS films are generally underdense with tensile stresses, while HiPIMS films had high compressive stresses ranging from 3 to 6 GPa due to the increased ion energy which causes atomic peening in the film.

In DCMS, independent control of E_i and J_i/J_{Me} can be achieved using tunable magnetically unbalanced magnetrons.¹⁴ Varying J_i/J_{Me} , while maintaining E_i constant at ≈ 20 –25 eV, during magnetron sputter deposition has been shown to be an effective method for controlling crystal quality and the microstructural evolution of epitaxial and polycrystalline TiN,^{15,16} Ti_{0.5}Al_{0.5}N,⁹ TaN,^{17,18} and ScN¹⁹ layers while introducing negligible concentrations of residual ion-induced defects and residual stress.

In this article, we summarize the results of an investigation of low-energy ion-irradiation effects on the microstructure and physical properties of HfN_x layers ($0.45 \leq x \leq 1.60$) grown on amorphous SiO₂ at $T_s = 350$ °C in mixed N₂/Ar discharges at a total pressure of 20 mTorr by UHV magnetically unbalanced reactive magnetron sputter deposition. The films, ≈ 500 nm thick, were grown under two sets of ion-irradiation conditions: (1) mild irradiation with

incident ion energy $E_i \approx 7$ eV and ion-to-Hf flux ratios $J_i/J_{Hf} = 1$ –3 and (2) intense irradiation with $E_i = 25$ eV and $J_i/J_{Hf} = 4$ –20. The HfN_x phases obtained with increasing x are hcp-structure α -Hf ($x \lesssim 0.6$), multiphase mixtures consisting of α -Hf, δ -HfN, ϵ -Hf₃N₂, and/or ζ -Hf₄N₃ ($0.6 \lesssim x \lesssim 0.9$), single phase δ -HfN ($0.9 \lesssim x \lesssim 1.3$), and mixtures of δ -HfN and higher nitrides ($x \gtrsim 1.3$).

Series-1 δ -HfN_x layers with $0.90 \lesssim x \lesssim 1.20$ exhibit an underdense structure with inter- and intracolumnar voids, mixed orientation, low in-plane stress ranging from +0.22 (tensile) to –0.44 GPa (compressive), and rough surface morphologies. However, Series-2 HfN_x layers in the same composition range have a dense microstructure with a strong 111-texture, compressive in-plane stress between –1.42 and –1.77 GPa, and smooth surfaces. In this composition range, the electrical resistivity ρ is lower and the hardness H is higher for Series-2 layers than for Series-1 due to the microstructure and texture evolution resulting from ion irradiation enhanced adatom surface mobilities.

For HfN_x layers with $1.20 \lesssim x \lesssim 1.60$, however, both Series-1 and -2 samples exhibit fully dense structures with complete 001 preferred orientation and compressive in-plane residual stress. For these 001-texture samples, changing the intensity of ion irradiation has little effect on microstructure, surface morphology, and physical properties.

II. EXPERIMENT

Polycrystalline HfN_x layers are grown in a load-locked multi-chamber UHV stainless-steel magnetically unbalanced magnetron sputter deposition system, described in detail in Ref. 13. The pressure in the sample introduction chamber is reduced to less than 5×10^{-8} Torr (7×10^{-6} Pa), using a 50 l s^{-1} turbomolecular pump (TMP), prior to initiating substrate exchange into the deposition chamber, which has a base pressure of 5×10^{-10} Torr (7×10^{-8} Pa), achieved using a 500 l s^{-1} TMP. The target is a 7.6-cm-diameter water-cooled Hf disk, 99.9% pure (the only detectable contaminant is Zr, the usual metallurgical impurity in Hf). Sputter deposition is carried out at a constant power of 150 W in mixed atmospheres consisting of Ar (99.9999% pure) and N₂ (99.999%) with a target-to-substrate separation of 6.5 cm. The gases are introduced through high precision solenoid valves, while the pressure is measured by a capacitance manometer and maintained constant with an automatic mass-flow controller.

The substrates are 500-nm-thick amorphous SiO₂ layers produced by thermally oxidizing $12 \times 10 \times 0.5 \text{ mm}^3$ Si(001) wafers. They are cleaned with successive rinses in ultrasonic baths of trichloroethane, acetone, ethanol, and de-ionized water and blown dry with dry N₂. The substrates are then mounted on resistively heated Ta platens using Mo clips and inserted into the sample introduction chamber for transport to the growth chamber where they are thermally degassed at 500 °C for 1 h. Immediately prior to initiating deposition, the target is sputter-etched for 5 min with a shutter shielding the substrate. The HfN_x layers are grown at $T_s = 350$ °C, including the contribution due to plasma heating. T_s is measured with a pyrometer calibrated by a thermocouple bonded to an HfN-coated SiO₂ substrate. Following deposition, the samples are allowed to cool below 100 °C before transferring them to the load-lock chamber, which is then backfilled with dry N₂.

16 October 2023 08:36:32

A pair of external Helmholtz coils with Fe pole pieces is utilized to controllably unbalance the magnetic circuit in the magnetron sputtering system through the addition of a uniform axial magnetic field B_{ext} in the region between the target and the substrate. This allows independent control of the energy and flux of ions incident at the growing film.¹⁴

Electrostatic probes are used to measure plasma characteristics in the vicinity of the substrate during film growth, following the procedure described in Refs. 14 and 20. The ion flux J_i , plasma potential V_p , and floating potential V_f are obtained from the current-voltage characteristics of a 6-mm-diameter stainless-steel disc probe mounted in a through-hole drilled in the center of a special substrate platen. The surface of the probe is co-incident with the substrate surface and is electrically isolated from the platen by a 0.25-mm vacuum gap. In this geometry, the actual current densities at the substrates are measured irrespective of the value of B_{ext} . To minimize edge effects, the probe and substrate platen are maintained at the same potential with respect to the grounded chamber.

The HfN_x layers, ≈ 500 nm thick, are deposited with N_2 fractions f_{N_2} ranging from 0.025 to 0.3 at the relatively high sputtering pressure of 20 mTorr (2.67 Pa), chosen to suppress kinetic energy transfer to the growing film by ions neutralized and backscattered from the target. Series-1 samples are deposited on electrically floating SiO_2 substrates with $B_{\text{ext}} = 0$, resulting in $E_i = e(|V_f - V_p|) \approx 7$ eV and $J_i/J_{\text{Hf}} = 1-3$, depending upon f_{N_2} , while Series-2 films are grown in a magnetically unbalanced mode with $B_{\text{ext}} = 180$ G and an applied bias V_s used to maintain the ion energy, $E_i = e(|V_s - V_p|)$, constant at 25 eV. These conditions result in $J_i/J_{\text{Hf}} = 4-20$ with increasing f_{N_2} .

Film compositions are determined by Rutherford backscattering spectrometry (RBS). The probe beam consists of 2 MeV He^+ ions incident at 22.5° relative to the sample surface normal with the detector set at a 150° scattering angle. The total accumulated ion dose is $100 \mu\text{C}$. Backscattered spectra are analyzed using the RUMP simulation program,²¹ and the uncertainty in reported N/Hf ratios is less than ± 0.03 . Combining the results of the ion probe measurements with RBS data for the total number of deposited Hf atoms yields values for the ion-to-Hf flux ratios J_i/J_{Hf} incident at the substrate.

The phase, microstructure, residual stress, and surface morphology of as-deposited HfN_x films are determined using a combination of x-ray diffraction (XRD), atomic force microscopy (AFM), and plan-view TEM. $\theta-2\theta$ and glancing angle (GA) XRD scans are obtained in the powder diffraction mode with a resolution of 0.01° 2θ using a Rigaku D-Max diffractometer, while in-plane stresses and relaxed lattice parameters are determined by the $\sin^2\psi$ technique²² using a four-circle Philips X-Pert diffractometer. Surface morphologies and roughnesses are quantified by AFM with a Digital Instruments Nanoscope II instrument operated in the tapping mode. Several $1 \times 1 \mu\text{m}^2$ scans are obtained for each sample using (001) n-type Si tips with radii of 10 nm. Plan-view TEM analyses are performed in a Philips CM12 microscope operated at 120 kV. TEM specimens are thinned by mechanical grinding from the backside to a thickness of $\approx 25 \mu\text{m}$. Final thinning to electron transparency is accompanied by ion milling using a 5 keV Ar^+ ion beam incident at 12° .

Four-point probe measurements are utilized to determine the room-temperature resistivities ρ of as-deposited HfN_x layers.

Hardnesses H and elastic moduli E are obtained from nanoindentation responses measured with a Hysitron TriboScope instrument attached to an AFM. The area function of the triangular Berkovich diamond tip is calibrated following the procedure described in Ref. 23 and the calibration is checked using epitaxial $\text{TiN}/\text{MgO}(001)$ layers of known hardness²⁴ and the same thickness as the HfN_x samples. The maximum load is varied from 0.05 to 9 mN with a minimum of 10 indent sequences for each load.

III. RESULTS AND DISCUSSION

A. Plasma probe measurements

Varying B_{ext} during the reactive magnetron sputter deposition of HfN_x dramatically alters the ion flux J_i incident at the growing film. In the case of layers deposited with $f_{\text{N}_2} = 0.05$, for example, probe measurements show that J_i increases from 9.1×10^{14} to $3.7 \times 10^{16} \text{ cm}^{-2} \text{ s}^{-1}$ (0.15 to 5.89 mA cm^{-2}) as B_{ext} is increased from -60 to $+180$ G. The positive direction of B_{ext} is defined as assisting the outer pole of the magnetron. Changes in B_{ext} over this range, however, have very little effect on the overall impedance of the magnetron discharge. At a constant target power of 150 W, the discharge voltage only increases from 302 V at $B_{\text{ext}} = -60$ G to 312 V at 180 G with no measurable change in the target sputtering rate. As a result, J_i/J_{Hf} can be varied from 0.13 with $B_{\text{ext}} = -60$ G to 5.29 with $B_{\text{ext}} = 180$ G for layers deposited with $f_{\text{N}_2} = 0.05$. The corresponding changes in the plasma potential V_p and floating potential V_f range from $V_p = -13.4$ to -20.4 V and $V_f = -19.4$ to -26.6 V.

Figure 1 summarizes the variation in J_i/J_{Hf} as a function of B_{ext} during magnetically unbalanced reactive magnetron sputter deposition of HfN_x layers grown with $f_{\text{N}_2} = 0, 0.05, 0.07, 0.10,$ and 0.20 . J_i/J_{Hf} increases with increasing f_{N_2} at all B_{ext} values. With $B_{\text{ext}} = 180$ G and no applied substrate bias, for example, J_i/J_{Hf} varies from 2.5 with $f_{\text{N}_2} = 0$ to 16.4 with $f_{\text{N}_2} = 0.20$, while the incident ion energy, $E_i = e(|V_f - V_p|)$, remains essentially constant at ≈ 7 eV.

16 October 2023 08:36:32

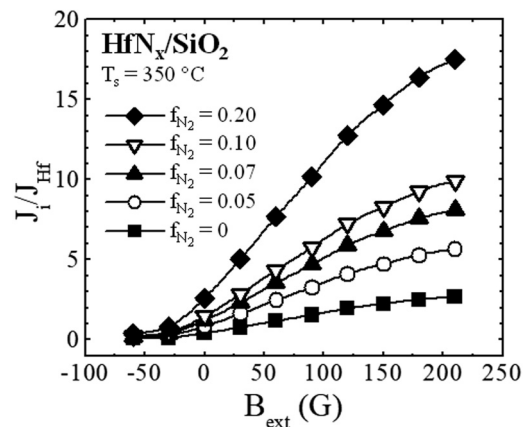


FIG. 1. Ion-to-Hf flux ratios J_i/J_{Hf} incident at the substrate as a function of the external magnetic field B_{ext} during magnetically unbalanced reactive magnetron sputter deposition of HfN_x in mixed N_2/Ar discharges at a total pressure of 20 mTorr.

From previous double-modulated glow discharge mass spectrometry measurements during the magnetron sputtering of Ti in Ar/N₂ mixtures,²⁵ the primary ions incident at the substrate over the f_{N_2} range from 0.100 to 0.275 are Ar⁺ (92–94%), Ar²⁺ (3–4%), and N₂⁺ (2–5%). For all gas mixtures, sputtered species represent less than 1% of the total ion population. The vast majority of the ions incident at the substrate and growing film during deposition experience the full substrate sheath potential E_s , since the mean free paths for Ar⁺ and N₂⁺ charge exchange collisions,²⁶ ≈ 6 and ≈ 8 mm, respectively, are much larger than the sheath width, estimated from the Child–Langmuir equation,²⁷ to be 0.3–0.5 mm.

B. HfN_x phase composition

HfN_x RBS results summarized in Fig. 2 show that the N/Hf ratio x continuously increases from 0.45 to 1.60 as f_{N_2} is increased from 0.025 to 0.30. Rapid changes in x with $f_{N_2} \leq 0.1$ correspond to increasing nitride coverage on the Hf target giving rise to a lower metal sputtering rate. In this f_{N_2} range, Fig. 2 shows that films grown with intense ion irradiation (Series-2 samples with $E_i = 25$ eV, $J_i/J_{Hf} = 4$ –20, and $B_{ext} = 180$ G) have slightly lower N concentration than those with mild ion irradiation (Series-1, $E_i \approx 7$ eV, $J_i/J_{Hf} = 1$ –3, and $B_{ext} = 0$). In contrast to the growth of TiN_x for which films remain essentially stoichiometric for f_{N_2} values between 0.04 and 1,²⁵ the HfN_x film composition x continues to increase smoothly from $x = 1$ at $f_{N_2} \approx 0.05$ to $x = 1.6$ at $f_{N_2} = 0.3$. We attribute this to the existence of N-rich phases²⁸ in the Hf–N system, while TiN is the terminal phase in the Ti–N system.

Figure 3 is a representative series of GA-XRD 2 θ scans, which are sensitive to the presence of small volume fractions of randomly oriented grains, from Series-1 HfN_x layers grown as a function of f_{N_2} under mild ion-irradiation conditions ($E_i \approx 7$ eV with $J_i/J_{Hf} = 1$ –3). The combination of RBS and XRD results shows that, for the growth conditions used in these experiments, the HfN_x phase obtained does not depend on the ion-irradiation intensity. Thus, we present diffraction data, for phase identification, from Series-1 layers only. Layers with N/Hf ratio $x \leq 0.60$ ($f_{N_2} \leq 0.03$) are single

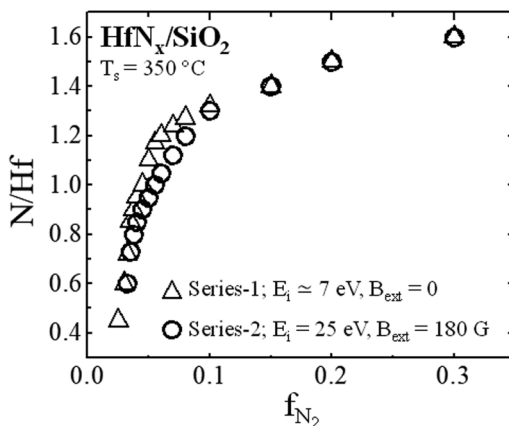


FIG. 2. N/Hf ratio vs N₂ discharge fraction f_{N_2} during the growth of HfN_x on SiO₂ at 350 °C.

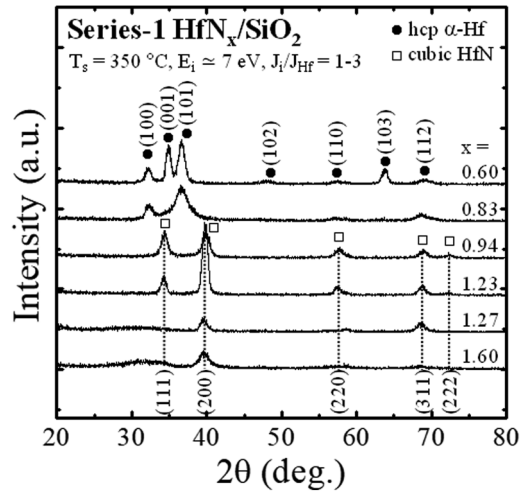


FIG. 3. GA-XRD 2 θ scans obtained from 500-nm-thick HfN_x layers grown as a function of x on SiO₂ at 350 °C with $E_i \approx 7$ eV and $J_i/J_{Hf} = 1$ –3.

phase with an α -Hf structure. Figure 3 is a typical XRD scan, in this case for a sample with $x = 0.60$, with peaks indexed as (100), (001), (101), (102), (110), (103), and (112). No compound HfN_x peaks are observed indicating that up to ≈ 37.5 at. % N can be dissolved in α -Hf under these growth conditions. This is well above the equilibrium solid solubility of 29 at. %.⁴ The XRD results show that with increasing x , α -Hf peak positions continuously shift to lower 2 θ values corresponding to higher N concentrations.

A small additional increase in N₂ ($0.0325 \leq f_{N_2} \leq 0.0375$) during the growth of Series-1 samples results in the formation of multiphase HfN_x layers with $0.72 \leq x \leq 0.88$. An example GA-XRD scan is given in Fig. 3 for an HfN_x layer with $x = 0.83$. In this composition range, the GA-XRD scans consist of broad diffraction features composed of overlapping peaks that cannot be deconvoluted. Thus, we also used selected-area electron diffraction (SAED) for phase identification. Figures 4(a)–4(d) are typical SAED patterns obtained from Series-1 HfN_x layers with $x = 0.83, 1.00, 1.23,$ and 1.60. In order to compare lattice spacings d for this set of samples, we used identical camera lengths and aligned the centers of the ring patterns in Figs. 4(a)–4(d). SAED results for HfN_{0.83} [Fig. 4(a)] exhibit broad features that correspond to d values ranging from 0.226 nm [using the (200) δ -HfN diffraction ring] to 0.277 nm [using the (100) α -Hf ring]. According to the Hf–N phase diagram,⁴ four different phases— α -Hf, ϵ -Hf₃N₂, ζ -Hf₄N₃, and δ -HfN—can exist in this composition range. The two intermediate phases, ϵ -Hf₃N₂ and ζ -Hf₄N₃, are complex rhombohedral stacking variants consisting of hcp α -Hf and δ -HfN with more than ten diffraction rings, many overlapping, in this d -spacing range.^{29,30}

The GA-XRD scans obtained from Series-1 layers with $0.94 \leq x \leq 1.23$ ($0.04 \leq f_{N_2} \leq 0.07$) contain (111), (200), (220), (311), and (222) NaCl-structure HfN_x diffraction peaks indicating that, under these growth conditions, the single-phase field extends from $x \approx 0.94$ to 1.23. This is similar to the case for epitaxial HfN_x(001) layers in a previous work³¹ in which the compound phase field

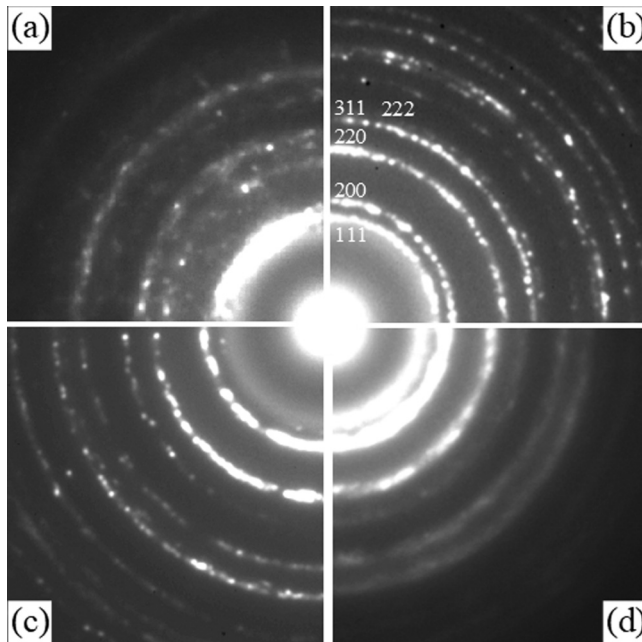


FIG. 4. SAED patterns obtained from 500-nm-thick Series-1 HfN_x layers grown on SiO_2 at 350°C : (a) $x = 0.83$, $E_i \approx 7$ eV, and $J_i/J_{\text{Hf}} \approx 1$, (b) $x = 1.0$, $E_i \approx 7$ eV, and $J_i/J_{\text{Hf}} \approx 1$, (c) $x = 1.23$, $E_i \approx 7$ eV, and $J_i/J_{\text{Hf}} \approx 2$, and (d) $x = 1.50$, $E_i \approx 7$ eV, and $J_i/J_{\text{Hf}} \approx 3$.

ranged from 0.80 to 1.20. The SAED patterns in Figs. 4(b) ($x = 1.00$) and 4(c) ($x = 1.23$) are consistent with the GA-XRD scans, revealing a single-phase NaCl structure. Note that the (111) and (222) diffraction rings are missing in Fig. 4(c) since $\text{HfN}_{1.23}$ layers have a fully developed (001) texture as discussed below.

Series-1 HfN_x layers grown with $0.08 \leq f_{\text{N}_2} \leq 0.5$ ($1.27 \leq x \leq 1.60$) exhibit the same δ -HfN GA-XRD peaks together with an additional broad peak at $2\theta \approx 31^\circ$ [which likely contains a component of the δ -HfN (111) peak at $2\theta = 34.3^\circ$] arising from the presence of an N-rich second phase. Thus, Series-1 HfN_x layers with $1.27 \leq x \leq 1.60$ are two-phase mixtures consisting primarily of δ -HfN together with N-rich inclusions. The presence of an N-rich second phase at high x values is also observed in epitaxial $\text{HfN}_x(001)$ layers.³¹ The SAED pattern from $\text{HfN}_{1.60}$ in Fig. 4(d) exhibits a broad diffraction ring at $d \approx 0.28$ nm stemming from the N-rich phase.

GA-XRD and SAED results are summarized in Fig. 5 as an HfN_x phase map plotted as a function of the N_2 fraction f_{N_2} during film growth versus layer composition x . There are four regions: single phase α -Hf ($x \lesssim 0.6$); a multiphase field consisting of α -Hf, δ -HfN, ε - Hf_3N_2 , and/or ζ - Hf_4N_3 ($0.6 \lesssim x \lesssim 0.9$); single phase δ -HfN ($0.9 \lesssim x \lesssim 1.3$); and a two-phase field composed of δ -HfN and an N-rich phase ($x \gtrsim 1.3$).

C. HfN_x microstructure and texture evolution

In this section, we summarize the results of an investigation of the effects of ion irradiation on microstructural and texture

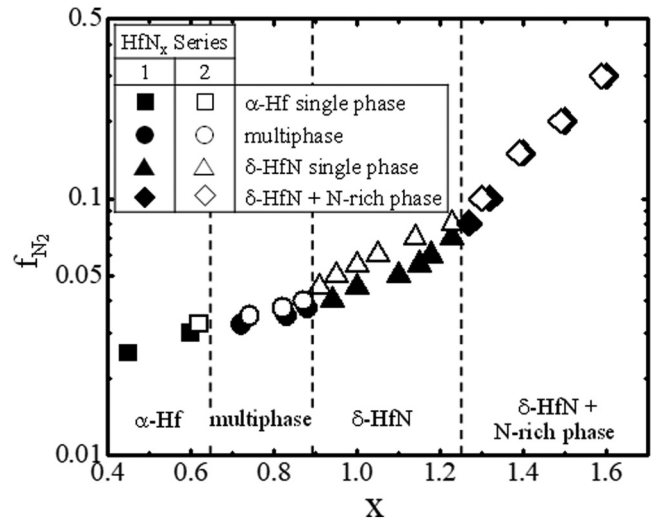


FIG. 5. Growth phase map plotted as f_{N_2} vs x , showing the phase composition of HfN_x layers grown on SiO_2 at 350°C by reactive magnetron sputter deposition in mixed N_2/Ar discharges.

evolution in HfN_x layers, which are either single-phase NaCl structures ($0.9 \lesssim x \lesssim 1.3$) or have δ -HfN as the primary phase ($1.3 \lesssim x \lesssim 1.6$). Figures 6(a) and 6(b) show typical θ - 2θ XRD scans from HfN_x layers grown on SiO_2 at 350°C with mild (Series-1) and intense (Series-2) ion irradiation, respectively. The intensities of $x = 1.23$ and 1.32 Series-1 and $x = 1.30$ Series-2 layers are reduced by $0.2\times$ to decrease peak overlap.

For Series-1 layers, XRD θ - 2θ scans [Fig. 6(a)] and pole figure (not shown) results demonstrate that HfN_x films with $0.94 \leq x \leq 1.18$ exhibit mixed orientation with an intense (111) peak and smaller (002), (022), and (113) peaks, while films with $x \geq 1.23$ have a complete 001 texture. In contrast, Series-2 HfN_x films with $0.87 \leq x \leq 1.05$ grown with intense ion irradiation [Fig. 6(b)] have a strong 111 texture, while layers with $x \geq 1.23$ exhibit a complete 001 texture. Figure 7, which shows normalized plots of (111) and (002) XRD peak intensities [$I_{111}/(I_{111} + I_{002} + I_{022} + I_{113})$ and $I_{002}/(I_{111} + I_{002} + I_{022} + I_{113})$] as a function of x , summarizes the HfN_x texture-transition results as a function of film composition x and ion-irradiation intensity. Both Series-1 and Series-2 HfN_x films can be divided into three composition regimes: low x ($0.9 \lesssim x \lesssim 1.1$), medium x ($1.1 \lesssim x \lesssim 1.2$), and high x ($1.2 \lesssim x \lesssim 1.6$). As x increased, the HfN_x texture changed from mixed to 001 for Series-1 layers and from 111 to 001 for Series-2 films. For medium x values, both Series-1 and Series-2 HfN_x films are in the texture-transition region (see Table 1).

HfN_x layers with $0.9 \lesssim x \lesssim 1.6$ were analyzed using the XRD $\sin^2\psi$ technique²² in order to estimate residual in-plane stresses σ and to determine relaxed HfN_x lattice parameters a_o as a function of x . The lattice parameter a_ψ , where ψ is the azimuthal angle between the texture plane and (hkl) planes, was obtained from θ - 2θ XRD scans in several directions. Depending on which was the

16 October 2023 08:36:32

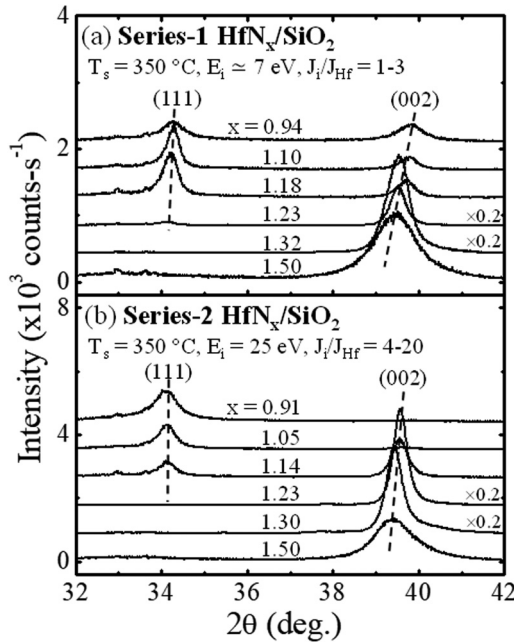


FIG. 6. XRD θ - 2θ scans obtained from 500-nm-thick HfN_x layers grown on SiO_2 at 350 °C with (a) $E_i \approx 7$ eV and $J_i/J_{\text{Hf}} = 1-3$ and (b) $E_i = 25$ eV and $J_i/J_{\text{Hf}} = 4-20$.

strongest XRD peak intensity in a given layer, we chose either 111 or 001 as the surface normal. Thus, ψ is determined from the equations

$$\cos \psi = \frac{h + k + l}{[3(h^2 + k^2 + l^2)]^{1/2}} \quad (1)$$

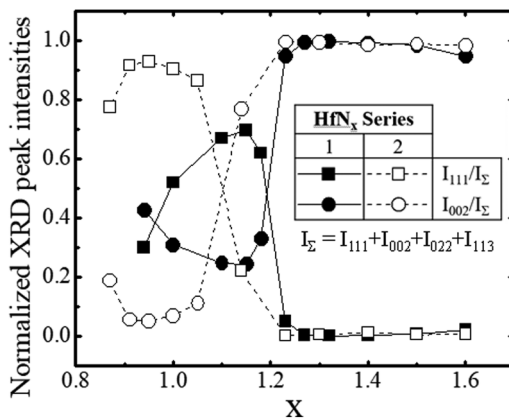


FIG. 7. Normalized intensities of the (111) and (002) HfN_x XRD peaks in Fig. 6 as a function of x .

TABLE I. Summary of texture, microstructure, residual stress, and surface roughness of Series-1 and Series-2 HfN_x layers grown as a function of x .

x	Series-1	Series-2
Low ($0.9 \lesssim x \lesssim 1.1$)	<ul style="list-style-type: none"> Mixed texture Underdense structure Low tensile stress Rough surface 	<ul style="list-style-type: none"> 111 texture Dense structure Compressive stress Smooth surface
Medium ($1.1 \lesssim x \lesssim 1.2$)	<ul style="list-style-type: none"> Mixed texture Underdense structure Low compressive stress Rough surface 	<ul style="list-style-type: none"> Mixed texture Dense structure Compressive stress Smooth surface
High ($1.2 \lesssim x \lesssim 1.6$)	<ul style="list-style-type: none"> 001 texture Dense structure Compressive stress Median roughness 	<ul style="list-style-type: none"> 001 texture Fully dense structure High compressive stress Median roughness

for 111 textured HfN_x layers and

$$\cos \psi = \frac{l}{(h^2 + k^2 + l^2)^{1/2}} \quad (2)$$

for 001 textured HfN_x layers. From these relationships, (111), (1 $\bar{1}$ 1), (200), (220), (311), (3 $\bar{1}$ 1), and (3 $\bar{1}$ $\bar{1}$) θ - 2θ diffraction peaks are obtained with $\psi = 0^\circ, 70.6^\circ, 54.7^\circ, 35.3^\circ, 29.5^\circ, 58.5^\circ$, and 80.0° for 111 layers, while (111), (002), (022), (113), and (311) peaks are acquired with $\psi = 54.7^\circ, 0^\circ, 45^\circ, 25.2^\circ$, and 72.5° for 001 layers. The in-plane stress σ and a_o are related to measured a_ψ values through the equation

$$a_\psi = a_o + \frac{a_o \sigma}{E_{hkl}} [(1 + \nu_{hkl}) \sin^2 \psi - 2\nu_{hkl}] = \delta \sin^2 \psi + \xi, \quad (3)$$

where ν_{hkl} and E_{hkl} are the Poisson ratio and elastic modulus of the film in the $[hkl]$ direction.

We did not evaluate either the Poisson ratio or the orientation dependence of the elastic modulus of polycrystalline HfN_x . Thus, we have used an elastic modulus $E(x)$ obtained from nanoindentation measurements, discussed below, and taken ν to be 0.29 (Ref. 32) for all layers, irrespective of orientation. We estimate that the maximum uncertainties introduced by ν in determining σ and a_o are only ± 0.3 GPa and ± 0.0005 nm, respectively. σ and a_o values are obtained through the slope (δ) and intercept (ξ) of least-square fits of a_ψ versus $\sin^2 \psi$ plots using the relationships

$$a_o = \xi + \frac{2\delta\nu}{1+\nu}, \quad (4)$$

and

$$\sigma = \frac{\delta E}{2\delta\nu + (1+\nu)\xi}. \quad (5)$$

16 October 2023 08:36:32

σ and a_o values calculated from the results, using Eqs. (4) and (5), are plotted as a function of x in Figs. 8(a) and 8(b). Series-1 HfN_x layers with $0.9 \lesssim x \lesssim 1.2$ grown under mild ion irradiation have low in-plane residual stresses σ between +0.22 GPa (tensile) and -0.44 GPa (compressive). However, films of the same composition grown under intense ion irradiation (Series-2) are under compressive stresses ranging from -1.42 to -1.77 GPa. Based on the θ - 2θ XRD results discussed above, the film texture changes from mixed orientation to 111 texture with increasing ion-irradiation intensity in this composition range. For the 001 texture HfN_x layers with $1.2 \lesssim x \lesssim 1.6$, both Series-1 and Series-2 films are under compressive stresses, -1.18 to -1.98 GPa for Series-1 and -1.78 to -2.78 GPa for Series-2 layers.

The film/substrate differential thermal contraction stress due to cooling from $T_s = 350^\circ\text{C}$ to room temperature is given by $\sigma_T = [E_{\text{HfN}} / (1 - \nu_{\text{HfN}})](\alpha_{\text{HfN}} - \alpha_{\text{Si}})\Delta T$, where $\alpha_{\text{HfN}} = 6.9 \times 10^{-6} \text{K}^{-1}$ (Ref. 33) and $\alpha_{\text{Si}} = 2.59 \times 10^{-6} \text{K}^{-1}$ (Ref. 34) are the thermal expansion coefficients of HfN and Si (the oxide layer is too thin to have a significant effect), resulting in $\sigma_T \approx +0.52$ GPa tensile. Therefore, the compressive components of the residual stress in HfN_x films originate from ion bombardment during the deposition process. Series-2 HfN_x layers grown with intense low-energy ion irradiation have higher compressive stresses than Series-1 films over the entire composition range.

The relaxed lattice parameters $a_o(x)$ of single-phase $\delta\text{-HfN}_x$ layers are essentially constant at 0.4529 ± 0.0001 nm for Series-1 and 0.4531 ± 0.0001 nm for Series-2 layers over a wide range in

composition, $0.9 \lesssim x \lesssim 1.2$. However, as x exceeds 1.23, in 001-texture HfN_x , $a_o(x)$ increases continuously to $a_o = 0.4552$ nm for Series-1 and 0.4554 nm for Series-2 layers with $x = 1.60$. These $a_o(x)$ results are quite different than those of epitaxial $\text{HfN}_x(001)$ described in Ref. 31, for which a_o decreases linearly with x . We attribute the increase in $a_o(x)$ for polycrystalline HfN_x to N incorporation in interstitial sites, whereas in the epitaxial layers, excess N results in antisite defects. The variation in $a_o(x)$ trends arises from the large difference in deposition temperatures: 350°C for polycrystalline layers versus 650°C for epitaxial layers.³¹ The probability of trapping N in interstitial sites is relatively low at a higher growth temperature.

Figures 9(a) and 9(b) are plots of a_o versus x for Series-1 and Series-2 HfN_x layers as-deposited and after annealing at 700°C for 1 h in vacuum ($P \approx 10^{-8}$ Torr). The anneals resulted in a decrease in the N concentration x and the relaxed lattice parameter a_o . We attribute this to a loss of N interstitials, both by filling anion vacancies and by diffusing to the surface where they are lost by recombinative desorption. While a_o increases with x , due to the presence of N interstitials, for as-deposited layers, a_o for annealed films either remains essentially constant with x (Series-1) or decreases slightly with increasing x (Series-2). The $a_o(x)$ results for annealed polycrystalline HfN_x layers are consistent with those of as-deposited epitaxial $\text{HfN}_x(001)$, grown at 650°C .³¹ That is, in annealed HfN_x layers with $x > 1$, the primary defects are N antisites and Hf vacancies, both of which decrease a_o .

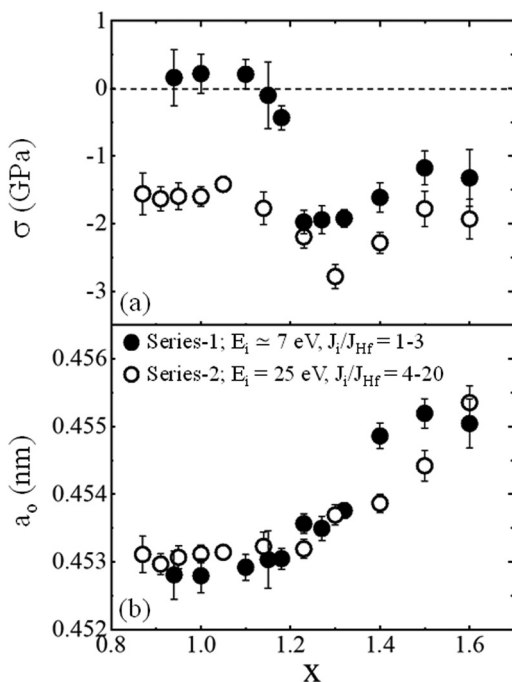


FIG. 8. (a) In-plane residual stresses σ and (b) relaxed lattice parameters a_o determined from $\sin^2\psi$ XRD measurements of HfN_x layers grown as a function of x on SiO_2 at 350°C .

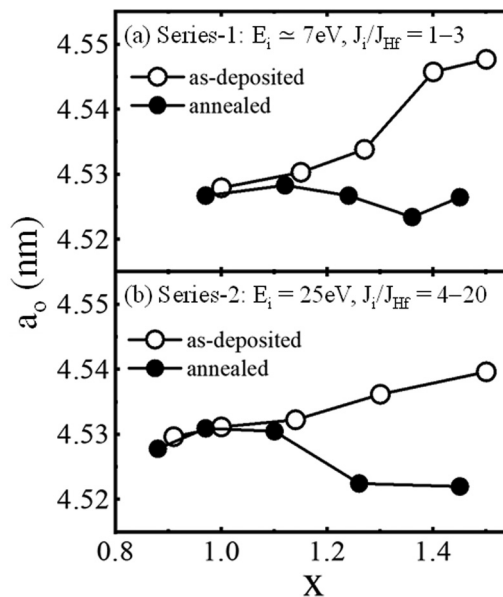


FIG. 9. Relaxed lattice parameters a_o determined from $\sin^2\psi$ XRD measurements of HfN_x layers grown as a function of x on SiO_2 with (a) $E_i \approx 7 \text{ eV}$ and $J_i/J_{\text{Hf}} = 1-3$ and (b) $E_i = 25 \text{ eV}$ and $J_i/J_{\text{Hf}} = 4-20$ before and after vacuum annealing at 700°C for 1 h.

Figures 10(a)–10(d) are typical plan-view TEM micrographs illustrating differences in HfN_x film microstructure as a function of composition and ion-irradiation conditions: (a) $x = 1.0$ (Series-1), (b) $x = 1.0$ (Series-2), (c) $x = 1.27$ (Series-1), and (d) $x = 1.24$ (Series-2). The absence of Moiré fringes indicates that all films have a columnar microstructure. Based on the XRD results discussed above, the layers shown in Fig. 10 have (a) mixed orientation and low tensile stress, (b) 111 texture and compressive stress, (c) 001 texture and compressive stress, and (d) 001 texture and high compressive stress.

The Series-1 HfN layer in Fig. 10(a), deposited with $E_i \approx 7$ eV and $J_i/J_{\text{Hf}} \approx 1$, exhibits an underdense structure due to competitive growth between grains with different orientations. The relatively low growth temperature ($T_s = 350$ °C corresponds to a homologous temperature $T_s/T_m = 0.17$, where T_m is the HfN melting point in K⁴ that leads to low adatom mobilities, resulting in kinetic roughening^{35–37} as the tops of protruding grains capture sputtered atoms at higher rates, while atomic shadowing blocks deposition at the valleys between grains. This gives rise to an underdense structure with both inter- and intracolumnar voids and no strong preferred orientation.

In contrast, the Series-2 HfN layer in Fig. 10(b), grown with $E_i = 25$ eV and $J_i/J_{\text{Hf}} \approx 6$, has a dense structure with a strong 111 texture and a compressive in-plane stress. The densification is due to ion irradiation enhanced adatom mobilities resulting in less kinetic roughening and, hence, decreased atomic shadowing. Under these intense ion irradiation and low f_{N_2} growth conditions, Hf

adatoms are strongly adsorbed on all high-index surfaces. However, Hf adatom mobilities are lower on (111) surfaces, where they have three backbonds, than on (001) surfaces with which they form only one backbond. Thus, adatom diffusivities and potential energies are higher on 001-oriented grains than on 111 grains and Hf adatoms have a higher chance of becoming trapped on 111 grains where they have a longer residence time. Consequently, 111 grains expand at the expense of the 001 grains, giving rise to the development of a 111-preferred orientation. Average grain sizes $\langle d \rangle$ of the underdense and dense stoichiometric HfN layers in Figs. 10(a) and 10(b) are 38 ± 18 and 41 ± 17 nm, respectively.

Figures 10(c) and 10(d) are plan-view TEM images from HfN_x samples having the strongest 001 texture in Series-1 ($x = 1.27$) and Series-2 ($x = 1.24$) layers. Both films exhibit a fully dense structure with a complete 001 texture and compressive in-plane stress. The only significant difference between the images in Figs. 10(c) and 10(d) is grain size with $\langle d \rangle = 48 \pm 15$ nm for the Series-1 layer and 62 ± 12 nm for the Series-2 layer. The higher grain size for the Series-2 layer is also due to ion irradiation enhanced adatom surface mobilities compared to the Series 1 layers. In contrast to HfN_x with $0.9 \lesssim x \lesssim 1.2$ for which ion-irradiation intensity controls texture evolution, the steady state atomic N coverage θ_{N} is of primary importance in this composition range and ion irradiation plays only a secondary role. For these high f_{N_2} growth conditions, the correspondingly high incident N_2^+ ion fluxes during film growth provide a continuous source of atomic N which can chemisorb on 001 grains ([001] is a nonpolar direction in the NaCl structure), but not on N-terminated 111 grains.^{38,39} Thus, θ_{N} on 001 grains increases with increasing f_{N_2} and $J_{\text{N}_2^+}/J_{\text{Hf}}$ while θ_{N} remains at a constant N-terminated value on 111 grains. This has the important consequence of decreasing cation mean free paths on (001) surfaces due to capture by N adatoms to form HfN_i ($i = 1$ to 4) admolecules which are more strongly bonded to the surface than Hf adatoms, and therefore, have lower surface mobilities. That is, in the presence of a sufficient atomic N source, the effective 001 adatom potential energy decreases below that on 111. Consequently, the net flux of cations from 001 to 111 oriented grains is reversed under high f_{N_2} conditions ($f_{\text{N}_2} > 0.07$), resulting in the development of 001 texture from the earliest stage of film growth. Under these conditions, due to the lack of competitive growth, even mild ion irradiation [e.g., $E_i \approx 7$ eV and $J_i/J_{\text{Hf}} \approx 2$ for the $\text{HfN}_{1.27}$ film in Fig. 10(c)] suppresses kinetic roughening and related atomic shadowing during deposition.

AFM results are used to provide a quantitative measure of HfN_x surface morphology as a function of x and ion irradiation. Figures 11(a)–11(d) are typical $1 \times 1 \mu\text{m}^2$ AFM images of the HfN_x layers corresponding to Figs. 10(a)–10(d). The 500-nm-thick underdense Series-1 $\text{HfN}_{1.0}$ layer in Fig. 11(a) is extremely rough with a surface width $\langle w \rangle$, equivalent to the root-mean-square (rms) roughness, of 2.74 nm, while the dense Series-2 111-oriented $\text{HfN}_{1.0}$ film [Fig. 11(b)] is much flatter with $\langle w \rangle = 0.57$ nm. The 001-textured Series-1 $\text{HfN}_{1.27}$ layer in Fig. 11(c) and Series-2 $\text{HfN}_{1.24}$ film in Fig. 11(d) exhibit intermediate surface roughnesses with $\langle w \rangle = 0.92$ and 1.02 nm, respectively.

$\langle w \rangle$ is plotted as a function of x for both Series-1 and Series-2 samples in Fig. 12. For understoichiometric HfN_x layers, $\langle w \rangle$ values

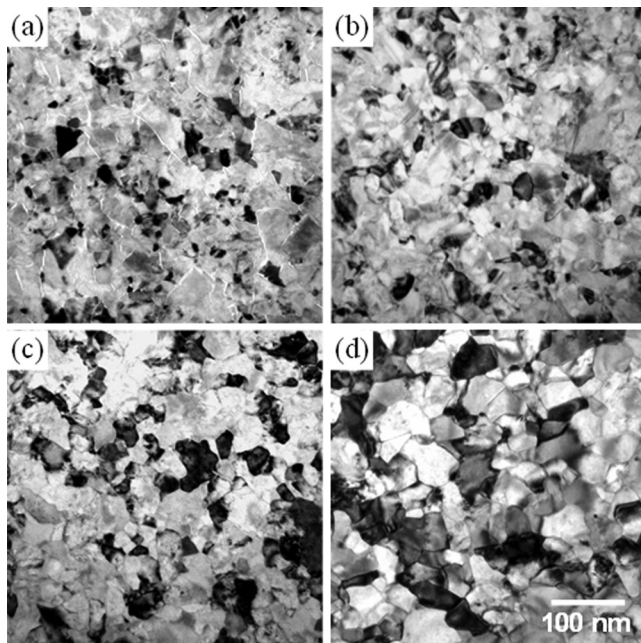


FIG. 10. Bright-field plan-view TEM images from HfN_x layers grown on SiO_2 at 350 °C: (a) $x = 1.0$, $E_i \approx 7$ eV, and $J_i/J_{\text{Hf}} \approx 1$, (b) $x = 1.0$, $E_i = 25$ eV, and $J_i/J_{\text{Hf}} \approx 6$, (c) $x = 1.27$, $E_i \approx 7$ eV, and $J_i/J_{\text{Hf}} \approx 2$, and (d) $x = 1.24$, $E_i = 25$ eV, and $J_i/J_{\text{Hf}} \approx 9$.

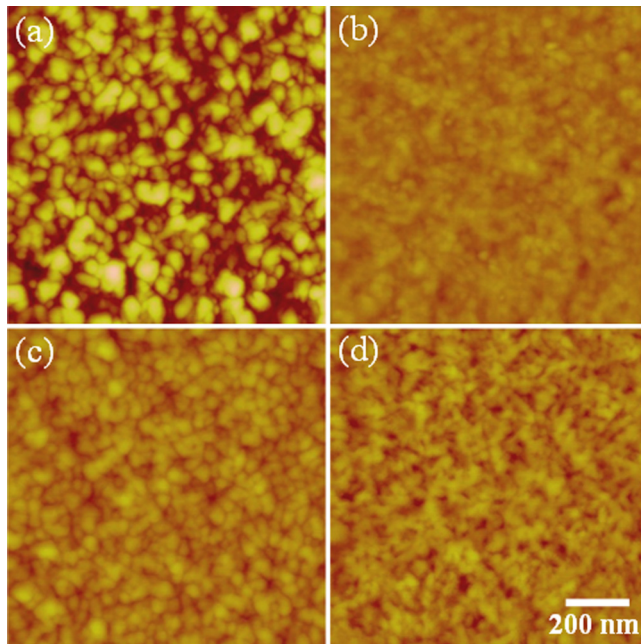


FIG. 11. AFM images, $1 \times 1 \mu\text{m}^2$, from HfN_x layers grown on SiO_2 at 350°C : (a) $x = 1.0$, $E_i \approx 7 \text{ eV}$ and $J_i/J_{\text{Hf}} \approx 1$, (b) $x = 1.0$, $E_i = 25 \text{ eV}$, and $J_i/J_{\text{Hf}} \approx 6$, (c) $x = 1.27$, $E_i \approx 7 \text{ eV}$, and $J_i/J_{\text{Hf}} \approx 2$, and (d) $x = 1.24$, $E_i = 25 \text{ eV}$, and $J_i/J_{\text{Hf}} \approx 9$.

continuously decrease from $\approx 3 \text{ nm}$ for metallic hcp $\alpha\text{-Hf}$ phase samples at $x \approx 0.45$ to 0.7 nm for multiphase films with $x \approx 0.9$. However, for single-phase $\delta\text{-HfN}_x$ layers with compositions $0.9 \lesssim x \lesssim 1.2$, $\langle w \rangle$ values ($0.6\text{--}0.8 \text{ nm}$) for Series-2 layers, are much lower than those ($2.0\text{--}2.7 \text{ nm}$) for Series-1 films. The rough surface morphology for single-phase Series-1 HfN_x layers is due to kinetic

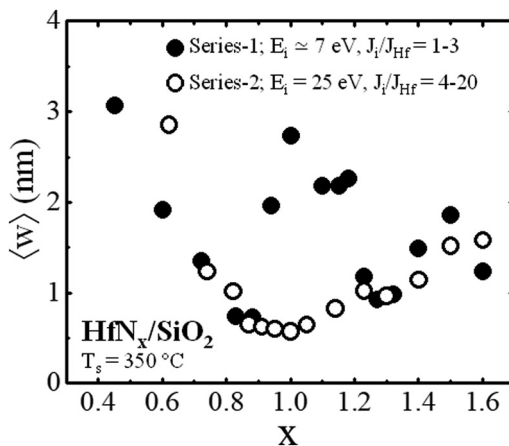


FIG. 12. Surface widths $\langle w \rangle$ of HfN_x layers grown as a function of x on SiO_2 at 350°C .

roughening during film growth. Under these mild ion-irradiation conditions, atomic shadowing caused by low adatom mobilities leads to rough film surfaces with self-organized growth mounds separated by deep surface trenches⁴⁰ leading to a porous columnar microstructure and mixed orientation. However, over the same composition range, HfN_x layers grown under intense ion irradiation (Series-2) have dramatically lower surface roughness values. The smooth surface morphology is attributed to less pronounced kinetic roughening due to ion irradiation enhanced surface mobilities resulting in film densification, and hence, decreased atomic shadowing.

For 001-oriented overstoichiometric HfN_x layers with $1.2 \lesssim x \lesssim 1.6$, both the Hf adatom diffusion length and the effective nucleation length decrease dramatically with increasing θ_N (due to increasing f_{N_2} and, hence, x) on (001) surfaces, and thus, $\langle w \rangle$ values increase continuously with x . Over this composition range, Series-1 $\langle w \rangle$ values, which range from 0.9 to 1.8 nm , are essentially equal to those of Series-2 samples since additional ion irradiation has little effect on the microstructure and texture evolution.

Table 1 summarizes texture, microstructure, residual stress, and surface roughness results for Series-1 and Series-2 HfN_x layers as a function of x .

D. Physical properties of HfN_x versus x

Figure 13 shows the variation in the room-temperature electrical resistivity ρ of Series-1 and Series-2 HfN_x layers as a function of x . The overall composition dependence of the resistivity of NaCl-structure single-phase $\delta\text{-HfN}_x$ ($0.9 \lesssim x \lesssim 1.3$), with the lowest value at $x = 1$ and ρ increasing with both $x < 1$ and $x > 1$, is typical for TM-nitrides, including the other members of the IVB-VA group, TiN_x ^{3,28} and ZrN_x .²⁸ The resistivity values obtained at stoichiometric composition are $69.7 \mu\Omega \text{ cm}$ for Series-1 and $35.2 \mu\Omega \text{ cm}$ for Series-2 layers. These ρ values for polycrystalline HfN layers are higher than that of single-crystal $\text{HfN}(001)$, $\rho = 14.2 \mu\Omega \text{ cm}$,⁴¹ but much lower than that of the previously

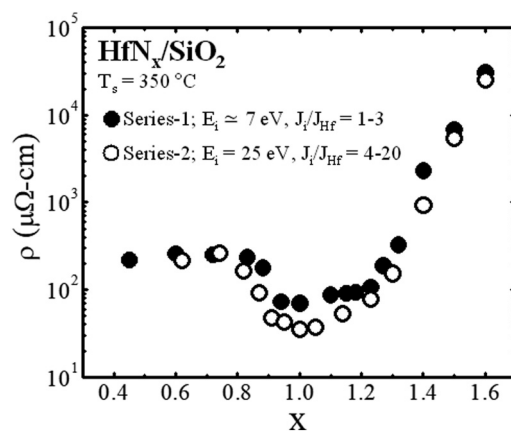


FIG. 13. Room-temperature resistivities ρ of HfN_x layers grown as a function of x on SiO_2 at 350°C .

16 October 2023 08:36:32

reported polycrystalline HfN layers, $\rho = 225 \mu\Omega \text{ cm}$,^{28,42} grown with no applied ion irradiation, and $\times 2$ lower than the value reported for epitaxial films deposited at temperatures below 150 °C by HiPIMS.¹² The increase in ρ for single-phase δ -HfN_x as the composition deviates from stoichiometry is primarily due to scattering from point defects, including N and Hf vacancies, N interstitials, and antisite defects as described in Ref. 41.

For α -HfN samples, ρ increases with x , with little difference between Series-1 and Series-2 samples, up to the N composition corresponding to the solubility limit, $x \approx 0.6$, where $\rho \approx 260 \mu\Omega \text{ cm}$. In the multiphase (α -HfN + δ -HfN + ϵ -Hf₃N₂ and/or ζ -Hf₄N₃) region with $0.6 \lesssim x \lesssim 0.9$, ρ remains essentially constant at $\approx 250 \mu\Omega \text{ cm}$ with $x < 0.8$ and starts to decrease with $x > 0.8$ as the volume fraction of δ -HfN increases. For $x > 1$, ρ increases again to $\approx 30\,000 \mu\Omega \text{ cm}$ with $x = 1.6$. The presence of a high resistivity N-rich second phase contributes to the dramatic increase in ρ with $x \gtrsim 1.3$.

Over the entire composition range for which the NaCl structure δ -HfN is either the only phase ($0.9 \lesssim x \lesssim 1.3$) or the primary phase ($1.3 \lesssim x \lesssim 1.6$), Series-2 layers have ρ values that are 15–50% lower than Series-1 films. The electron mean free path obtained from measured room-temperature resistivities ρ , using an estimated Fermi velocity of $2 \times 10^8 \text{ cm/s}$ (Ref. 43), ranges from $\approx 1 \text{ nm}$ with $x = 1.6$ to $\approx 20 \text{ nm}$ with $x = 1.0$. These values are well below the average grain sizes, 30–70 nm, as shown in Fig. 10. Thus, charge scattering from grain boundaries and intercolumnar voids does not significantly affect electron transport. Instead, point defects—including vacancies, interstitials, and antisite substitutions—control carrier scattering in these films. The lower ρ values observed in Series-2 layers are again due to ion irradiation enhanced surface mobilities resulting in lower defect densities.

The hardnesses H and elastic moduli E of HfN_x layers are determined from nanoindentation measurements, following the procedure described in Ref. 24. Multiple loading cycles with maximum peak loads that range from 0.05 to 9 mN are used. H values are extracted from data corresponding to maximum displacements of less than 100 nm. At larger displacements, substrate effects influence the results, giving rise to lower H values due to the relatively low hardness of SiO₂.

H values for Series-1 and Series-2 HfN_x layers as a function of x are plotted in Fig. 14. $H(x)$ for both sample sets increases in the α -HfN phase region with increasing N concentration and continues to increase into the multiphase region to reach a maximum of $31.7 \pm 1.2 \text{ GPa}$ for Series-1 and $37.5 \pm 1.2 \text{ GPa}$ for Series-2 layers with $x \approx 0.87$. Figure 15 is a plan-view TEM micrograph of this film with the highest hardness. The film appears fully dense with individual grains having a very distorted nanostructure due to the effects of intense ion irradiation. In addition, we observe in many grains alternating stripe contrast, which is similar to the one reported in substoichiometric TaN_x films with hardness above 40 GPa.^{18,44} Because x-ray diffraction indicates a mixture of δ -HfN and lower nitrides, we believe these stripes may indicate a self-organized nanolamellar structure consisting of coherent δ -HfN, ϵ -Hf₃N₂, and/or ζ -Hf₄N₃ layers similar to the reported results for TaN_x.^{18,44}

Over the composition range $0.8 \lesssim x \lesssim 1.2$, $H(x)$ values for Series-2 HfN_x layers are higher by 10%–25% than those of Series-1 films. For example, the hardness of Series-1 stoichiometric HfN is 21.7 GPa, while $H = 27.6 \text{ GPa}$ for Series-2 films. The increase in H

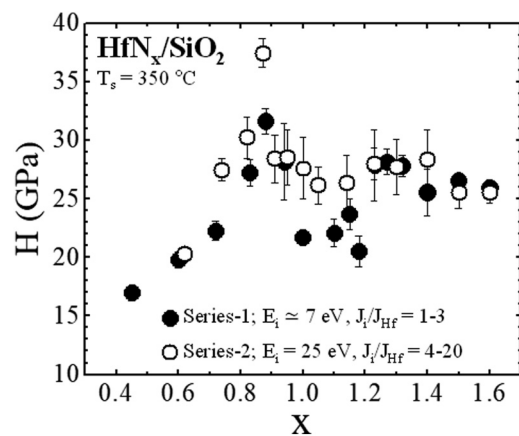


FIG. 14. Nanoindentation hardness H of HfN_x layers grown as a function of x on SiO₂ at 350 °C.

with increasing ion-irradiation intensity is due to a corresponding increase in film density as shown in the TEM results in Figs. 10(a) and 10(b). The porosity in Series-1 films allows increased inter- and intracolumnar deformation under nanoindentation load. Similar results, an increase in H due to film densification by intense ion irradiation, were reported for TiN_x,⁴⁵ CrN_x,⁴⁶ and TaN_x¹⁸ layers grown by reactive magnetron sputtering. An additional contribution to the increase in hardness is a continuous change in the residual stress, for example, from $\approx +0.2 \text{ GPa}$ tensile for Series-1 HfN to $\approx -1.6 \text{ GPa}$ compressive for Series-2 films, as shown in Fig. 8(a). Stress-induced hardening is often observed in

16 October 2023 08:36:32

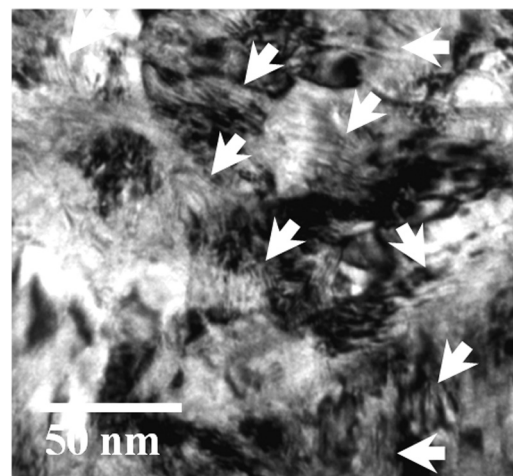


FIG. 15. Bright-field plan-view TEM image from HfN_{0.87} layer, grown on SiO₂ at 350 °C with $E_i = 25 \text{ eV}$ and $J_i/J_{\text{Hf}} \approx 5$, which exhibits the highest hardness of $37.5 \pm 1.2 \text{ GPa}$. Alternating stripe contrasts (Moiré fringes) are observed.

polycrystalline films⁴⁵ and is associated with an increased resistance to slip deformation at the nanoscale.

For the 001-textured HfN_x layers with $1.2 \lesssim x \lesssim 1.6$, H(x) values of Series-1 and Series-2 HfN_x are essentially equivalent and show very little variation as a function of x since all films have fully dense structures [see, for example, Figs. 10(c) and 10(d)]. Higher compressive stress in Series-2 HfN_x layers [see Fig. 8(a)] should result in higher hardness, but this effect is overcome by an overall increase in the grain size which decreases the hardness. H values for HfN_x with $1.4 \lesssim x \lesssim 1.6$, ≈ 26 GPa, are slightly lower than those with $1.2 \lesssim x \lesssim 1.4$, ≈ 28 GPa, primarily due to the increasing volume fraction of the N-rich second phase.

IV. CONCLUSIONS

Polycrystalline HfN_x layers with x ranging from 0.45 to 1.60 are grown on SiO₂ at T_s = 350 °C by UHV magnetically unbalanced reactive magnetron sputter deposition in mixed N₂/Ar discharges. We determined their phase composition, texture, microstructure, and physical properties as a function of x under both mild (Series-1; E_i ≈ 7 eV and J_i/J_{Hf} = 1–3) and intense (Series-2; E_i = 25 eV and J_i/J_{Hf} = 4–20) ion-irradiation conditions. For the growth conditions used in these experiments, the HfN_x phase composition does not depend on the ion-irradiation intensity. The observed HfN_x phase compositions in both Series-1 and Series-2 layers with increasing x are hcp-structure α -Hf ($x \lesssim 0.6$); multi-phase mixtures consisting of α -Hf, δ -HfN, ϵ -Hf₃N₂, and/or ζ -Hf₄N₃ ($0.6 \lesssim x \lesssim 0.9$); single phase δ -HfN ($0.9 \lesssim x \lesssim 1.3$); and mixtures of δ -HfN and higher nitrides ($x \gtrsim 1.3$).

Single-phase Series-1 HfN_x layers, $0.9 \lesssim x \lesssim 1.2$, grown under mild ion irradiation have an underdense columnar structure with inter- and intracolumnar voids, mixed orientation, low in-plane stress σ ranging from +0.2 GPa tensile to –0.4 GPa compressive, and a rough surface morphology with $\langle w \rangle > 2$ nm. These properties are due to competitive growth between grains of mixed orientations. Low adatom mobilities, resulting from the combination of a low growth temperature and relatively mild ion irradiation, give rise to the rapid development of kinetic roughening during film growth. However, Series-2 HfN_x layers with the same composition range exhibit dense structures with strong 111-texture, compressive in-plane stress of $\sigma \approx -1.6$ GPa, and smooth surface with $\langle w \rangle \approx 0.6$ nm due to the enhanced surface mobilities resulting in less kinetic roughening. Under intense low-energy ion-irradiation conditions, Hf adatom diffusivities and potential energies are lower on 111-oriented grains than on 001 grains, and, hence, 111 texture develops. As a result of ion-irradiation-induced microstructural evolution, lower resistivity and higher hardness are obtained in Series-2 layers. For stoichiometric HfN, ρ decreases from 69.7 to 35.2 $\mu\Omega$ cm and H increases from 22.1 to 27.4 GPa with increasing ion-irradiation intensity.

Both Series-1 and Series-2 HfN_x films with $1.2 \lesssim x \lesssim 1.6$ exhibit a fully dense structure with complete 001 texture and compressive in-plane residual stress, ≈ -2 GPa for Series-1 and ≈ -3 GPa for Series-2 layers. In contrast to HfN_x with $0.9 \lesssim x \lesssim 1.2$, for which ion-irradiation intensity controls microstructural and texture evolution, microstructure and texture evolution in HfN_x layers with $1.2 \lesssim x \lesssim 1.6$ is primarily controlled by the steady state atomic N

coverage θ_N and ion irradiation is only of secondary importance. θ_N on nonpolar 001 grains increases with increasing f_{N_2} and J_{N_2+}/J_{Hf} while θ_N remains at a constant N-terminated value on polar 111 grains. This reduces the Hf adatom diffusion length on 001 grains, and, hence, the effective 001 adatom potential energy decreases below that on 111. Since competitive growth is suppressed, the degree of kinetic roughening and atomic shadowing is greatly reduced. Consequently, HfN_x with $1.2 \lesssim x \lesssim 1.6$ exhibits 001 texture and a fully dense structure even under mild ion irradiation, and changing the ion-irradiation intensity has little effect on the physical properties, including ρ and H which are in the range up to $\approx 30\,000 \mu\Omega$ cm and ≈ 28 GPa, respectively, depending on x.

ACKNOWLEDGMENTS

This research was supported by the U.S. Department of Energy, Division of Materials Science, under Grant No. DEFG02-91ER45439 through the University of Illinois Materials Research Laboratory and was carried out in part in the Materials Research Laboratory Central Research Facilities, University of Illinois. This work was supported by the Korea Medical Device Development Fund grant funded by the Korea government (the Ministry of Science and ICT, the Ministry of Trade, Industry and Energy, the Ministry of Health & Welfare, the Ministry of Food and Drug Safety) (Project Nos. 1711194307 and RS-2020-KD000093). This work was supported by Priority Research Centers Program through the National Research Foundation of Korea (No. NRF-2019R1A6A1A11055660). This work was supported by the National Research Foundation of Korea (NRF) grant funded by the Korea government (MSIT) (No. RS-2023-00234581).

AUTHOR DECLARATIONS

Conflict of Interest

The authors have no conflicts to disclose.

Author Contributions

Hwan-Seok Seo: Conceptualization (equal); Formal analysis (lead); Investigation (lead); Methodology (lead); Writing – original draft (lead); Writing – review & editing (equal). **Taeyoon Lee:** Formal analysis (equal); Investigation (equal); Methodology (equal); Writing – review & editing (equal). **Hyungjun Kim:** Investigation (equal); Writing – review & editing (equal). **Ivan Petrov:** Conceptualization (equal); Project administration (equal); Supervision (lead); Writing – review & editing (equal). **J. E. Greene:** Conceptualization (equal); Project administration (equal); Supervision (lead); Writing – review & editing (equal).

DATA AVAILABILITY

The data that support the findings of this study are available from the corresponding author upon reasonable request.

REFERENCES

- ¹C. Stampfl, W. Mannstadt, R. Asahi, and A. J. Freeman, *Phys. Rev. B* **63**, 155106 (2001).
- ²A. Delin, O. Eriksson, R. Ahuja, B. Johansson, M. S. S. Brooks, T. Gasche, S. Auluck, and J. M. Wills, *Phys. Rev. B* **54**, 1673 (1996).

- ³J.-E. Sundgren, B.-O. Johansson, A. Rockett, S. A. Barnett, and J. E. Greene, in *Physics and Chemistry of Protective Coatings*, edited by J. E. Greene, W. D. Sproul, and J. A. Thornton (American Institute of Physics, New York, 1986), p. 95, AIP Conf. Ser. No. 149.
- ⁴T. B. Massalski, in *Binary Alloy Phase Diagrams*, edited by T. B. Massalski (ASM International, Metals Park, OH, 1990), p. 2090.
- ⁵J. E. Greene, S. A. Barnett, J.-E. Sundgren, and A. Rockett, in *Ion Beam Assisted Film Growth*, edited by T. Itoh (Elsevier, Amsterdam, 1988), Chap. 5.
- ⁶J. E. Greene, S. A. Barnett, J.-E. Sundgren, and A. Rockett, in *Plasma Surface Interactions and Processing of Materials*, edited by O. Auciello, A. Gras-Marti, J. A. Valles-Abaraca, and D. L. Flamm (Kluwer Academic, Amsterdam, 1990), p. 281, NATO ASI Series.
- ⁷I. Petrov, L. Hultman, J.-E. Sundgren, and J. E. Greene, *J. Vac. Sci. Technol. A* **10**, 265 (1992).
- ⁸G. Håkansson, J.-E. Sundgren, D. McIntyre, J. E. Greene, and W.-D. Münz, *Thin Solid Films* **153**, 55 (1987).
- ⁹F. Adibi, I. Petrov, J. E. Greene, L. Hultman, and J.-E. Sundgren, *J. Appl. Phys.* **73**, 8580 (1993).
- ¹⁰A. Anders, M. Panjan, R. Franz, J. Andersson, and P. Ni, *Appl. Phys. Lett.* **103**, 144103 (2013).
- ¹¹W. Tillmann, N. Dias, D. Stangier, M. Tolan, and M. Paulus, *Thin Solid Films* **669**, 65 (2019).
- ¹²M. Villamayor, J. Keraudy, T. Shimizu, R. Viloan, R. Boyd, D. Lundin, J. E. Greene, I. Petrov, and U. Helmersson, *J. Vac. Sci. Technol. A* **36**, 06151 (2018).
- ¹³D. Ö. Thorsteinsson and J. T. Gudmundsson, *AIP Adv.* **8**, 035124 (2018).
- ¹⁴I. Petrov, F. Adibi, J. E. Greene, W. D. Sproul, and W.-D. Münz, *J. Vac. Sci. Technol. A* **10**, 3283 (1992).
- ¹⁵J. E. Greene, J.-E. Sundgren, L. Hultman, I. Petrov, and D. B. Bergstrom, *Appl. Phys. Lett.* **67**, 2928 (1995).
- ¹⁶L. Hultman, J.-E. Sundgren, J. E. Greene, D. B. Bergstrom, and I. Petrov, *J. Appl. Phys.* **78**, 5395 (1995).
- ¹⁷C.-S. Shin, D. Gall, Y.-W. Kim, N. Hellgren, I. Petrov, and J. E. Greene, *J. Appl. Phys.* **92**, 5084 (2002).
- ¹⁸C.-S. Shin, Y.-W. Kim, N. Hellgren, D. Gall, I. Petrov, and J. E. Greene, *J. Vac. Sci. Technol. A* **20**, 2007 (2002).
- ¹⁹D. Gall, I. Petrov, N. Hellgren, L. Hultman, J. E. Sundgren, and J. E. Greene, *J. Appl. Phys.* **84**, 6034 (1998).
- ²⁰I. Petrov, V. Orlinov, I. Ivanov, and J. Kourtev, *Contrib. Plasma Phys.* **28**, 157 (1988).
- ²¹L. R. Doolittle, *Nucl. Instrum. Methods Phys. Res. Sect. B* **9**, 344 (1985).
- ²²I. C. Noyan and J. B. Cohen, *Residual Stresses* (Springer, New York, 1987).
- ²³W. C. Oliver and G. M. Pharr, *J. Mater. Res.* **7**, 1564 (1992).
- ²⁴H. Ljungcrantz, M. Odén, L. Hultman, J. E. Greene, and J.-E. Sundgren, *J. Appl. Phys.* **80**, 6725 (1996).
- ²⁵I. Petrov, A. Myers, J. E. Greene, and J. R. Abelson, *J. Vac. Sci. Technol. A* **12**, 2846 (1994).
- ²⁶A. V. Phelps, *J. Phys. Chem. Ref. Data* **20**, 557 (1991).
- ²⁷B. Chapman, *Glow Discharge Processes* (Wiley, New York, 1980), p. 108.
- ²⁸B. O. Johansson, H. T. G. Hentzell, J. M. E. Harper, and J. J. Cuomo, *J. Mater. Res.* **1**, 442 (1986).
- ²⁹*Inorganic Index to Powder Diffraction File* (Joint Committee on Powder Diffraction Standards, Swarthmore, PA, 1997), Card No. 23-1097.
- ³⁰*Inorganic Index to Powder Diffraction File* (Joint Committee on Powder Diffraction Standards, Swarthmore, PA, 1997), Card No. 24-0465.
- ³¹H.-S. Seo, T.-Y. Lee, I. Petrov, J. E. Greene, and D. Gall, *J. Appl. Phys.* **97**, 083521 (2005).
- ³²J. Tan *et al.*, *Phys. Status Solidi B* **254**, 1700063 (2017).
- ³³L. E. Toth, *Transition Metal Carbides and Nitrides* (Academic, New York, 1971), p. 7, and references therein.
- ³⁴*Quick Reference Manual for Silicon Integrated Circuit Technology*, edited by W. W. Beadle, J. C. C. Tsai, and R. D. Plummer (Wiley, New York, 1994), pp. 2–56.
- ³⁵J. E. Van Nostrand, S. J. Chey, M.-A. Hasan, D. G. Cahill, and J. E. Greene, *Phys. Rev. Lett.* **74**, 1127 (1995).
- ³⁶B. W. Karr, I. Petrov, P. Desjardins, D. G. Cahill, and J. E. Greene, *Surf. Coat. Technol.* **94–95**, 403 (1997).
- ³⁷N.-E. Lee, D. Cahill, and J. E. Greene, *Phys. Rev. B* **53**, 7876 (1996).
- ³⁸I. Petrov, P. B. Barna, L. Hultman, and J. E. Greene, *J. Vac. Sci. Technol. A* **21**, S117 (2003).
- ³⁹D. Gall, S. Kodambaka, M. A. Wall, I. Petrov, and J. E. Greene, *J. Appl. Phys.* **93**, 9086 (2003).
- ⁴⁰L. Hultman, L. R. Wallenberg, M. Shinn, and S. A. Barnett, *J. Vac. Sci. Technol. A* **10**, 1618 (1992).
- ⁴¹H.-S. Seo, T.-Y. Lee, J. G. Wen, I. Petrov, J. E. Greene, and D. Gall, *J. Appl. Phys.* **96**, 878 (2004).
- ⁴²B. O. Johansson, J.-E. Sundgren, and U. Helmersson, *J. Appl. Phys.* **58**, 3112 (1985).
- ⁴³N. W. Ashcroft and N. D. Mermin, *Solid State Physics* (Holt, Rinehart and Winston, New York, 1976), p. 36.
- ⁴⁴G. R. Lee, J. J. Lee, C.-S. Shin, I. Petrov, and J. E. Greene, *Thin Solid Films* **475**, 45 (2005).
- ⁴⁵D. S. Rickerby and P. J. Burnett, *Thin Solid Films* **157**, 195 (1988).
- ⁴⁶D. Gall, C.-S. Shin, T. Spila, M. Odén, M. J. H. Senna, J. E. Greene, and I. Petrov, *J. Appl. Phys.* **91**, 3589 (2002).